Modeling of kinematic hardening at large biaxial deformations in pearlitic rail steel

International Journal of Solids and Structures 130–131 (2018) 122–132

Contents lists available at ScienceDirect

International Journal of Solids and Structures

journal homepage: www.elsevier.com/locate/ijsolstr

Modeling of kinematic hardening at large biaxial deformations in pearlitic rail steel

Knut Andreas Meyer[a,*], Magnus Ekh[a], Johan Ahlström[b]

[a] Division of Material and Computational Mechanics, Department of Industrial and Materials Science, Chalmers University of Technology, Gothenburg, 412 96, Sweden

[b] Division of Engineering Materials, Department of Industrial and Materials Science, Chalmers University of Technology, Gothenburg, 412 96, Sweden

ARTICLE INFO

Article history:
Received 7 June 2017
Revised 30 August 2017
Available online 9 October 2017

Keywords:
Axial-Torsion
Pearlitic steel
Biaxial
Multiaxial
Finite strains

ABSTRACT

Using an Axial-Torsion testing machine, pearlitic R260 steel specimens are twisted until fracture under different axial loads. A well established framework for finite elastoplasticity with kinematic hardening is used to model the deformation of the specimens. In particular, we evaluate the ability of different kinematic hardening laws to predict the observed biaxial load versus displacement response. It is found that the combination of Armstrong–Frederick dynamic recovery and Burlet–Cailletaud radial evanescence saturation is efficient even for the large strains achieved in this study. The results are less conclusive on the appropriateness of replacing the Armstrong–Frederick with an Ohno–Wang type of kinematic hardening law.

1. Introduction

Large shear strains accumulate close to the running band of railway rails and wheels during service (see e.g. Alwahdi et al., 2013; Cvetkovski and Ahlström, 2013). The connection to crack initiation is well established, see Johnson (1989) for an overview. Additionally, plastic flow and wear cause changes in the geometry, altering the contact loading conditions. Hence, accurate constitutive models for cyclic large strain plasticity are important components for the prediction of the fatigue life of wheels and rails. This work considers experiments and modeling of cyclic large strain plasticity of one of the most common rail steels, the pearlitic grade R260.

The load on the rail consists of a large hydrostatic compressive stress due to the normal contact, and shear stresses mainly due to traction and cornering. Severe plastic deformation techniques, such as Plane Stress Local Torsion (PSLT), High Pressure Torsion (HPT) and Equal Channel Angular Pressing (ECAP), have been applied by several authors (e.g. Hohenwarter et al., 2011; Ivanisenko et al., 2002; Khoddam et al., 2014; Wetscher et al., 2007) to mimic these loading conditions. Significant strain localization occurs in PSLT testing which makes further characterization difficult. HPT testing has been particularly successful in obtaining a severely deformed microstructure under controlled laboratory conditions. While able to replicate the strains, the two latter processes are difficult to use for direct model evaluations due to the complex contact conditions. Several authors (e.g. Estrin et al., 2008; Wei et al., 2014; Larijani et al., 2015; Yoon et al., 2008; Kim, 2001; Draï and Aour, 2013) have simulated the HPT process, and Larijani et al. (2015) even simulated the extraction of specimens from the deformed disks and their uniaxial response. However, multiaxial loading of the extracted specimens is challenging, due to the limited size that can be extracted with a reasonable homogeneous deformation.

The first objective of this paper is to investigate the possibility of using an Axial-Torsion testing machine to obtain large shear strains in cylindrical test specimens. Such predeformed specimens can in future works be used in Low Cycle Fatigue (LCF) experiments, determining the influence of large strains on the multiaxial LCF behavior. This avoids the complicated contact conditions present in ECAP and HPT testing, and enables evaluation of the material response during large deformations. To investigate the potential to reach high shear strains, the amount of twisting that the specimens can endure before failure is evaluated for different axial loads.

The second objective of this paper is to identify appropriate cyclic plasticity models for modeling the large biaxial strains from the experiments. Many constitutive models for cyclic metal plasticity, such as the Chaboche model (Chaboche, 1986) and Ohno–Wang (Ohno and Wang, 1993a), are known to over-predict multiaxial ratcheting (e.g. Abdel-Karim, 2009; Bari and Hassan, 2002; Portier et al., 2000; Chen et al., 2005). Delobelle et al. (1995) suggested to use a linear combination of the Armstrong–Frederick dynamic recovery term and the radial evanescence term introduced by Burlet and Cailletaud (1986). This suggestion was

* Corresponding author.
E-mail address: knut.andreas.meyer@chalmers.se (K.A. Meyer).

https://doi.org/10.1016/j.ijsolstr.2017.10.007
0020-7683/

Table 1
% mass composition of the R260 steel, analyzed according to ASTM E 572, 1086 and 1029.

C	Si	Mn	P	S	Cr	Al	V	N	Cu
0.72	0.31	1.04	0.006	0.01	0.02	< 0.002	< 0.005	0.006	0.018

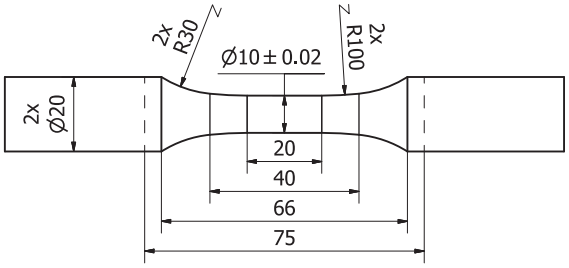

Fig. 1. Specimen dimensions in mm. Dashed lines indicate grip positions.

shown to solve some issues in modeling multiaxial ratcheting. Johansson et al. (2005a) formulated the combined Armstrong–Frederick and Burlet–Cailletaud rule using the hyperelasto-plastic framework from Wallin et al. (2003). Promising results were obtained in Johansson et al. (2005a) when this model was compared to the small strain test data from Hassan et al. (1992). These findings have not, however, been confirmed for large inelastic deformations. This is evaluated in the present study, where we investigate how well different kinematic evolution laws are able to predict the response for large shear strains.

It is commonly known that the yield surface distorts during plastic deformations (see e.g. Sung et al., 2011, and references therein). Several modeling approaches have proved successful at modeling this distortional hardening (e.g. Barthel et al., 2008; Harrysson et al., 2007; Pietryga et al., 2012), and much work has been conducted on the theoretical derivations of such models (e.g. Feigenbaum and Dafalias, 2007; Harrysson et al., 2007; Menzel and Steinmann, 2003; Plesek et al., 2010; Shi et al., 2014). However, the experiments in the present work cannot clearly differentiate between different yield surface evolutions. We therefore limit this study to investigate whether a kinematic hardening law with an isotropic yield surface can describe the mechanical response. The evaluation of the yield surface distortion is left for future work.

This paper is organized as follows:

- In Section 2 the experimental setup and results are presented.
- In Section 3 the modeling framework and the different kinematic evolution laws are described.
- In Section 4 the methodology for obtaining the set of material parameters that best fit the experimental data is presented.
- In Section 5 the ability of the different models to fit and predict the experimental results is evaluated. We also compare the residual shear stresses for different models.

2. Experiments

Test bars were extracted about 20 mm below the surface of new pearlitic R260 rails heads, with the material composition given in Table 1. The bars were turned between centers to the dimensions given in Fig. 1. A smooth transition with radius of 100 mm was used to minimize the strain concentration at the end of the gauge section. The tests were conducted on an Axial-Torsion MTS test rig, with load cell capacities of 100 kN and 1100 Nm, and a torsional stroke of 90 deg. To deform the specimens, the following load sequence was used

1. Ramp axial load
2. Rotate 90 deg in 60 s, maintaining the axial load
3. Relax the axial and the torsional load
4. Open lower grip, rotate back and close grip. Go to 1.

Failure was detected when the torque dropped 2 Nm below the maximum value during the current load cycle. No false failures were detected using this criterion, but some specimens with tensile axial load fractured completely at failure detection.

An MTS 632.80 extensometer with a 12 mm gauge length was used to obtain the initial Young's modulus E and shear modulus G accurately. As the extensometer range was limited to ±6 deg/12 mm, the machine piston positioning sensors were used to measure specimen deformations. To reduce the influence from the machine deformations, the stiffness of the machine was quantified and compensated for (See Appendix A for further details). To ensure consistent results, the grips were positioned 75 mm apart at the beginning of each experiment.

Table 2
Elastic material parameters and initial yielding.

Parameter	Value	Std. dev.	Unit	N_{tests}
E	212.0	0.5	GPa	9
G	80.5	0.5	GPa	3
$R_{p0.01}$	388.5	5.4	MPa	9
$R_{p0.05}$	466.6	6.2	MPa	9
$R_{p0.2}$	534.2	6.8	MPa	2

2.1. Elastic material parameters

The initial elastic material parameters were calibrated using the extensometer data from the first load cycle. For Young's modulus, nine specimens were available using the initial ramp of the axial load. This data was also used to obtain the yield limits. Only the three tests with zero axial load were used to calculate the shear modulus. The values of the elastic parameters and the yield limits are presented in Table 2. It should be noted that while the elastic parameters are rather certain, the yield limits show larger spread. This is expected as the yielding is not distinct, which is also reflected in the difference between the yield definitions.

2.2. Experimental results

The results in terms of specimen length changes and torque responses for different axial loads are shown in Fig. 2. There is a strong influence of the axial loading on the torque response, which is mainly due to the nonlinear geometrical effect. For a nominal axial stress $\bar{P}_a = -500$ MPa the specimen diameter increases uniformly by approximately 12%, and the overall length decreases by about 7.5 mm. The initial torque is highest for zero axial load, followed by $\bar{P}_a = \pm 250$ MPa, see Fig. 2b. The torque increases faster for the compressive axial loads as the diameter starts to increase. For tensile axial loads, the diameter decreases uniformly and the torque quickly saturates. The behavior described above is mainly a result of material hardening and geometric changes.

From Fig. 2 it is clear that the amount of twist a specimen can withstand before failure is increasing significantly with the axial compressive stress. The amount of surface shear strain increases even more, due to the shortening of the specimen and the increase of gauge diameter. Higher compressive stresses than 600 MPa were not used in order to avoid buckling during twisting.

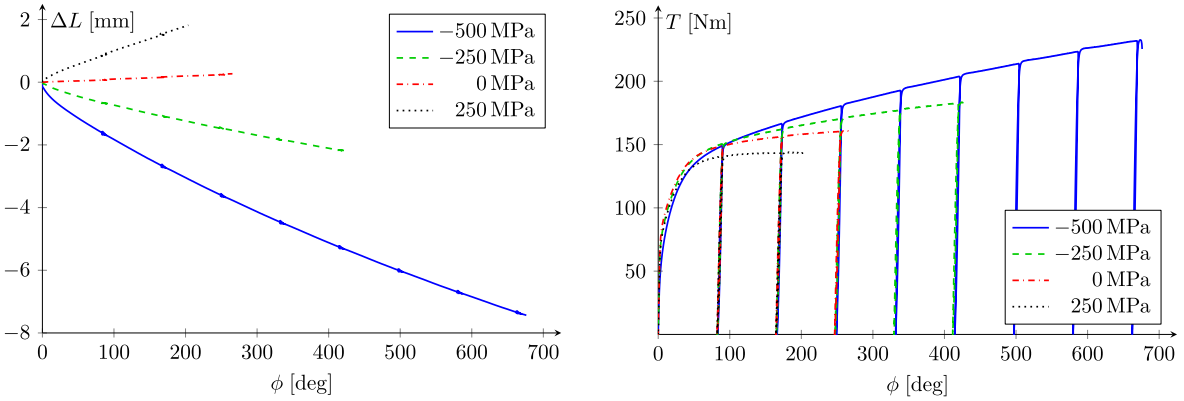

(a) Change of specimen length (b) Torque response

Fig. 2. Test results at different nominal axial stresses, $\bar{P}_a$.

3. Material modeling

In this paper we adopt a thermodynamically consistent hyperelasto-plastic modeling framework based on Wallin et al. (2003). Meyer and Ekh (2017) showed that this framework is equivalent to the framework introduced by Dettmer and Reese (2004), inspired by the work of Lion (2000). Vladimirov et al. (2008) further investigated the numerical implementation of this framework and Zhu et al. (2013) adapted it to the Ohno–Karim (Abdel-Karim and Ohno, 2000) kinematic evolution law. By introducing variations on the kinematic evolution equations, various combinations of small strain models are extended to the finite strain framework.

3.1. Base model

The multiplicative decomposition of the deformation gradient $\boldsymbol{F} = \boldsymbol{F}_e\boldsymbol{F}_p$ is adopted. Kinematic hardening is introduced via the kinematic hardening variable $\boldsymbol{F}_{k,i}$ ($\bar{\bar{\boldsymbol{F}}}$ in Wallin et al. (2003)) for each back-stress $i = 1, \dots, N_{back}$ and isotropic hardening with the scalar k (cf. Larijani et al., 2013). We define the deformation tensors $\boldsymbol{C}_e$ and $\boldsymbol{c}_{k,i}$:

$$\boldsymbol{C}_e := \boldsymbol{F}_e^t\boldsymbol{F}_e, \quad \boldsymbol{c}_{k,i} := \boldsymbol{F}_{k,i}^{-t}\boldsymbol{F}_{k,i}^{-1} \tag{1}$$

The Helmholtz free energy Ψ is assumed additively decomposed into an elastic part (Ψ_e), kinematic hardening parts ($\Psi_{k,i}$) and an isotropic hardening part (Ψ_{iso}) according to Larijani et al. (2013):

$$\Psi = \Psi_e(\boldsymbol{C}_e) + \sum_{i=1}^{N_{back}} \Psi_{k,i}\left(\boldsymbol{c}_{k,i}\right) + \Psi_{iso}(k) \tag{2}$$

Using the shorthand notation $I_{3\bullet} := \det(\bullet)$ the specific formulations of the free energies are written as:

$$\Psi_e(\boldsymbol{C}_e) := \frac{1}{2}G\left(\mathrm{tr}\left(I_{3C_e}^{-1/3}\boldsymbol{C}_e\right) - 3\right) + \frac{1}{2}K\left(I_{3C_e}^{1/2} - 1\right)^2 \tag{3}$$

$$\Psi_{k,i}(\boldsymbol{c}_{k,i}) := \frac{1}{2}H_{k,i}\left(\mathrm{tr}\left(I_{3c_{k,i}}^{-1/3}\boldsymbol{c}_{k,i}\right) - 3\right) \tag{4}$$

$$\Psi_{iso}(k) := \tfrac{1}{2}H_{iso}k^2 \tag{5}$$

Where G and K are the elastic shear and bulk moduli, while $H_{k,i}$ and H_{iso} are the kinematic and isotropic hardening moduli.

The Mandel stress $\boldsymbol{M}$, the Mandel back-stress $\boldsymbol{M}_{k,i}$ and the isotropic hardeing stress κ are of Neo–Hookean type and derived from the Helmholtz free energy:

$$\boldsymbol{M} := 2\boldsymbol{C}_e\frac{\partial\Psi_e}{\partial\boldsymbol{C}_e} = GI_{3C_e}^{-1/3}\boldsymbol{C}_e^{dev} + K\left(I_{3C_e} - \sqrt{I_{3C_e}}\right)\boldsymbol{I} \tag{6}$$

$$\boldsymbol{M}_{k,i} := 2\boldsymbol{c}_{k,i}\frac{\partial\Psi_{k,i}}{\partial\boldsymbol{c}_{k,i}} = H_{k,i}I_{3c_{k,i}}^{-1/3}\boldsymbol{c}_{k,i}^{dev} \tag{7}$$

$$\kappa := -\tfrac{\partial\Psi_{iso}}{\partial k} = -H_{iso}k \tag{8}$$

Here, we note that the Mandel back-stress $\boldsymbol{M}_{k,i}$ is deviatoric. The von Mises effective stress in Eq. (9) with the reduced Mandel stress $\boldsymbol{M}_{red}$ is used to formulate the yield function Φ in Eq. (11), where Y_0 is the initial yield limit. Using the reduced Mandel stress $\boldsymbol{M}_{red}$ in Eq. (9) is equivalent to using the reduced Kirchhoff stress $\boldsymbol{\tau}_{red} = \boldsymbol{F}_e\boldsymbol{M}_{red}\boldsymbol{F}_e^{-1}$.

$$f(\boldsymbol{x}) := \sqrt{\frac{3}{2}}\sqrt{\left(\boldsymbol{x}^t\right)^{dev} : \left(\boldsymbol{x}\right)^{dev}} \tag{9}$$

$$\boldsymbol{M}_{red} := \boldsymbol{M} - \textstyle\sum_{i=1}^{N_{back}}\boldsymbol{M}_{k,i} \tag{10}$$

$$\Phi := f(\boldsymbol{M}_{red}) - (Y_0 + \kappa) \leq 0 \tag{11}$$

We adopt an associative evolution of $\boldsymbol{F}_p$ and non-associative evolution of the hardening variables ($\boldsymbol{F}_{k,i}$ and k), whereby the plastic multiplier $\dot{\lambda}$ is introduced:

$$\dot{\boldsymbol{F}}_p\boldsymbol{F}_p^{-1} = \boldsymbol{L}_p = \dot{\lambda}\frac{\partial\Phi}{\partial\boldsymbol{M}} = \dot{\lambda}\frac{3}{2}\frac{\left(\boldsymbol{M}_{red}^t\right)^{dev}}{f(\boldsymbol{M}_{red})} \tag{12}$$

$$\dot{\boldsymbol{F}}_{k,i}\boldsymbol{F}_{k,i}^{-1} = \boldsymbol{L}_{k,i} =: \dot{\lambda}\boldsymbol{v}_{k,i}^* \tag{13}$$

$$\dot{k} = -\dot{\lambda}\left(1 - \frac{\kappa}{\kappa_\infty}\right) \tag{14}$$

The isotropic hardening is the standard exponentially saturating model (cf. Chaboche, 1986) such that $\kappa \to \kappa_\infty$. The Eqs. (12)–(14) are solved in a standard fashion using the backward Euler approximation along with the KKT-conditions ($\dot{\lambda}\Phi = 0,\ \dot{\lambda} \geq 0,\ \Phi \leq 0$). As noted by Vladimirov et al. (2008) this method is prone to numerical errors for large time steps. The influence of the length of the time steps is therefore evaluated in Appendix B to ensure that the numerical error is sufficiently small.

The model variations can be differentiated by the evolution of the kinematic hardening variables according to Eq. (13). The complete model is obtained by setting $\boldsymbol{\nu}^*_{\mathrm{k},i} = \boldsymbol{\nu}^{\mathrm{XX}}_{\mathrm{k},i}$ where XX denotes the initials used to identify each model in the following subsections.

3.2. Armstrong–Frederick dynamic recovery term (AF)

In Wallin et al. (2003) an Armstrong–Frederick (Frederick and Armstrong, 2007) type model was adopted. It was noted that only the symmetric part of $\boldsymbol{L}_{\mathrm{k},i}$ contributes to the dissipation, and the model flexibility was increased by adding a non-dissipative part to $\boldsymbol{\nu}^*_{\mathrm{k},i}$. Following the work of Johansson et al. (2005b); Larijani et al. (2013) we do not consider this addition, whereby the evolution law becomes

$$\boldsymbol{\nu}^{\mathrm{AF}}_{\mathrm{k},i} := -\boldsymbol{\nu} + \frac{3}{2}\frac{\boldsymbol{M}^{\mathrm{t}}_{\mathrm{k},i}}{Y_{\mathrm{k},i}} \tag{15}$$

where $Y_{\mathrm{k},i}$ is the effective back-stress saturation value and $\boldsymbol{\nu} := \frac{\partial \Phi}{\partial \boldsymbol{M}}$.

3.3. Burlet–Cailletaud radial evanescence term (BC)

As mentioned previously, several authors have found that the Chaboche model is unable to describe multiaxial behavior accurately. This was confirmed for the above formulation by Johansson et al. (2005b). Delobelle et al. (1995) suggested to introduce a linear combination of the radial evanescence term from Burlet and Cailletaud (1986) and the Armstrong–Frederick dynamic recovery term. Formulated in the current framework, following Johansson et al. (2005b), the evolution law for kinematic hardening becomes:

$$\boldsymbol{\nu}^{\mathrm{BC}}_{\mathrm{k},i} := -\boldsymbol{\nu} + \delta\frac{3}{2}\frac{\boldsymbol{M}^{\mathrm{t}}_{\mathrm{k},i}}{Y_{\mathrm{k},i}} + (1-\delta)\left(\frac{\boldsymbol{M}_{\mathrm{k},i} : \boldsymbol{\nu}}{Y_{\mathrm{k},i}}\right)\boldsymbol{\nu} \tag{16}$$

where the parameter δ controls the amount of Armstrong–Frederick versus Burlet–Cailletaud type of kinematic hardening. The radial evanescence term in Eq. (16) is basically the dynamic recovery term projected onto the direction of plastic flow $\boldsymbol{\nu}$. As noted by e.g. Bari and Hassan (2002) the BC radial evanescence term is equal to the AF dynamic recovery for proportional stress, the von Mises yield function and small strains. In general, this is not exactly fulfilled for the large strain formulation considered here.

3.4. Ohno–Wang model (OW)

Ohno and Wang (1993a) proposed two models, of which the second, which is used here, was a generalization of the first. This model has been shown to work well for uniaxial ratcheting (see e.g. Ohno and Wang, 1993b; Brommesson et al., 2015). Formulating the second Ohno–Wang model in terms of the Mandel stress, we extend the model to finite strains:

$$\boldsymbol{\nu}^{\mathrm{OW}}_{\mathrm{k},i} := -\boldsymbol{\nu} + \frac{3}{2}\frac{\boldsymbol{M}^{\mathrm{t}}_{\mathrm{k},i}}{Y_{\mathrm{k},i}}\left(\frac{f(\boldsymbol{M}_{\mathrm{k},i})}{Y_{\mathrm{k},i}}\right)^{m_i}\left\langle\frac{\boldsymbol{\nu} : \boldsymbol{M}_{\mathrm{k},i}}{f(\boldsymbol{M}_{\mathrm{k},i})}\right\rangle \tag{17}$$

The additional material parameter m_i controls how abruptly the saturation starts. Letting $m_i \to \infty$ gives a linear hardening until saturation is reached, followed by a constant back-stress. Additionally, the evolution of the back-stress differs between plastic loading or plastic unloading through the use of the Macaulay brackets $\langle\bullet\rangle$.

3.5. Ohno–Wang with radial evanescence (OB)

Although the Ohno–Wang model incorporates a multiaxial dependence through the contraction $\boldsymbol{\nu}:\boldsymbol{M}_{\mathrm{k},i}$, it has still been reported to overpredict the ratcheting for multiaxial loading (Chen et al., 2005). Chen et al. (2003) combined the second Ohno–Wang model with the Burlet–Cailletaud radial evanescence term, and this model is formulated within the considered finite strain framework as:

$$\boldsymbol{\nu}^{\mathrm{OB}}_{\mathrm{k},i} := -\boldsymbol{\nu} + \frac{\langle\boldsymbol{\nu} : \boldsymbol{M}_{\mathrm{k},i}\rangle}{Y_{\mathrm{k},i}}\left(\frac{f(\boldsymbol{M}_{\mathrm{k},i})}{Y_{\mathrm{k},i}}\right)^{m_i}\left(\delta\frac{3\boldsymbol{M}^{\mathrm{t}}_{\mathrm{k},i}}{2f(\boldsymbol{M}_{\mathrm{k},i})} + (1-\delta)\boldsymbol{\nu}\right) \tag{18}$$

The first two factors in the last term give the saturation, while the last factor gives the direction of saturation, controlled by the parameter δ in a similar way as in Eq. (16). Note that both terms in the last factor has are normalized, i.e. they do not influence the magnitude of $\boldsymbol{\nu}^{\mathrm{OB}}_{\mathrm{k},i}$.

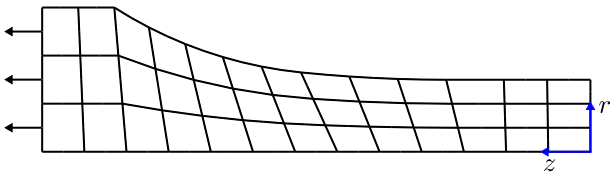

Fig. 3. Finite element discretization of one half specimen using 8 node axisymmetric reduced integration elements with twist. The loads and displacements are applied at the left end, and symmetric/antisymmetric boundary conditions are applied in the center (right). A right-hand $r-\phi-z$ cylindrical coordinate system is used.

4. Material parameter identification

Due to the heterogeneous strain field within the specimens, a finite element model with implicit time integration is used to simulate the experiments, see Fig. 3. The model is used in an iterative optimization algorithm to calibrate the material model, and reducing the computational cost is therefore important. A mesh convergence study that was conducted, showed that the depicted mesh gave sufficiently accurate results for the optimization (see Appendix B for details). Furthermore, the sensitivity to the size of the time steps is investigated in Appendix B. It is found that 40 steps for the axial ramp, 200 steps for the twisting and 20 steps for the unloading are sufficient for an accurate description of the deformation. This many steps is also used to ensure the global convergence in each time step.

The optimization procedure seeks to find the material parameter values that minimize the differences between the simulations and experiments in terms of the axial displacement and torque. The difference is evaluated for the load steps of type 2, in the load sequence described in Section 2. For a given load step i with evaluated data point j, the measured quantities are the torque T^{E}_{ij}, the axial displacement $\Delta L^{\mathrm{E}}_{ij}$ and the rotation ϕ^{E}_{ij}. The simulated values are described as functions, $T^{\mathrm{S}}_{ij} = T^{\mathrm{S}}_i(\phi^{\mathrm{E}}_{ij})$ and $\Delta L^{\mathrm{S}}_{ij} = \Delta L^{\mathrm{S}}_i(\phi^{\mathrm{E}}_{ij})$, obtained through linear interpolation from the closest simulated time increments. Before being used to evaluate the difference, each quantity $x^{\bullet}_{ij} = \{T^{\mathrm{E}}_{ij}, T^{\mathrm{S}}_{ij}, \Delta L^{\mathrm{E}}_{ij}, \text{ or} \Delta L^{\mathrm{S}}_{ij}\}$ is scaled according to:

$$\hat{x}^{\bullet}_{ij} := \frac{x^{\bullet}_{ij} - \min_j(x^{\mathrm{E}}_{ij})}{\max_j(x^{\mathrm{E}}_{ij}) - \min_j(x^{\mathrm{E}}_{ij})}\alpha_x \tag{19}$$

The factors $\alpha_T = 7.0$ and $\alpha_{\Delta L} = 1.0$ denote scale factors for torque and axial displacement. In each step, the scaled axial displacement is almost a straight line from 1 to 0, while the majority of the torque curve is located at the top 10% of the scaled output. It is therefore necessary to put more emphasis on the torque response to obtain a good balance between the contributions to the error from each curve. Further discussion on the influence of α_T and $\alpha_{\Delta L}$ is given in Section 5.1. The objective function for step i and

Table 3
Realistic interval for material parameters.

Parameter p	$p_{\min}$	$p_{\max}$	Unit
Y_0	0.3	0.8	GPa
H	0.5	12.0	GPa
Y_∞	0.8	2.0	GPa
δ	0.0	1.0	–
$r_{\mathrm{m},i}$	0.0	1.0	–
$r_{\mathrm{s},i}$	0.0	1.0	–
m_i	0.0	4.0	–

quantity x is calculated according to

$$E_i^x := \frac{1}{\sqrt{N_\mathrm{p}}}\sqrt{\sum_{j=1}^{N_\mathrm{p}}\left(\hat{x}_{ij}^{\mathrm{E}} - \hat{x}_{ij}^{\mathrm{S}}\right)^2} \tag{20}$$

where $N_\mathrm{p} \approx 600$ is the number of evaluated points. The complete objective function is created by summing the square of errors from all N_p load sequences:

$$E_{\mathrm{TOT}} := \frac{1}{\sqrt{N_\mathrm{s}}}\sqrt{\sum_{i=1}^{N_\mathrm{s}}\left(\left(E_i^T\right)^2 + \left(E_i^{\Delta L}\right)^2\right)} \tag{21}$$

The material parameters that are used in the optimization algorithm, are reformulated from Section 3. One linear back-stress with $H_\mathrm{k} = 10$ MPa is first fixed to ensure numerical stability. We then introduce ratios that allows, for example, to change the amount of isotropic hardening without modifying the total hardening modulus. The new material parameter set (E, K, Y_0, δ, H, Y_∞, $r_{\mathrm{m},i}$, $r_{\mathrm{s},i}$ and m_i) is introduced according to:

$$H := H_{\mathrm{iso}} + \sum_{i=1}^{N_\mathrm{b}} H_{\mathrm{k},i} \tag{22}$$

$$Y_\infty := Y_0 + \kappa_\infty + \sum_{i=1}^{N_\mathrm{b}} Y_{\mathrm{k},i} \tag{23}$$

$$r_{\mathrm{m},i} := \frac{H_{\mathrm{k},i}}{H} \tag{24}$$

$$r_{\mathrm{s},i} := \frac{Y_{\mathrm{k},i}}{(Y_\infty - Y_0)} \tag{25}$$

where N_b is the number of back-stresses excluding the linear back-stress.

The parameter space described in Table 3 is sampled with 200 points, using a Latin hypercube. Following Ekh (2001) we choose the $3N$ points with lowest E_{TOT} for each model, where N is the number of optimized material parameters. Using these points as starting guesses, the optimization procedure is performed using a Nelder–Mead Simplex algorithm (Lagarias et al., 1998). Attempts outside the permissible interval of material parameters from Table 3 are penalized by returning a value ten times the current minimum. Using this permissible interval $p_{\min} \le p \le p_{\max}$ for the material parameters, they are scaled ($\hat{p} \in [0, 1]$) according to:

$$\hat{p} := \frac{p - p_{\min}}{p_{\max} - p_{\min}} \tag{26}$$

The material parameters are identified for an experiment with the nominal axial stress $\bar{P}_\mathrm{a} = -500$ MPa.

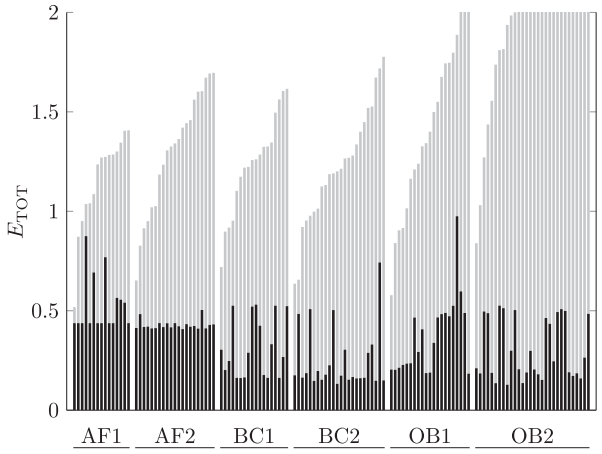

Fig. 4. Black bars show the converged E_{TOT} (objective function value) and the total height show E_{TOT} for the initial guesses. To improve readability, values above 2 are excluded. The models are designated by their initials and the number of back-stresses N_b.

5. Results

5.1. Optimization results

In Fig. 4 the initial and converged objective function values for each optimization run are presented. For the AF model with one back-stress (AF1) the lowest objective function value is obtained for several initial starting guesses. Hence, a global optimum seems to have been identified for this model. A slight improvement in the objective function value is found when increasing the number of back-stresses (AF2). In this case, the best runs do not arrive at the same objective function value, but they are still sufficiently similar to the AF1 to conclude that adding multiple back-stresses is not so efficient. The results when using the BC models (combined Armstrong–Frederick and Burlet–Cailletaud saturation) and the OB models (combined Ohno–Wang and Burlet–Cailletaud saturation), show that the objective function value can be significantly reduced. This shows that the inclusion of the Burlet–Cailletaud radial evanescence is effective for fitting the behavior at large biaxial strains. For both the BC and OB models, there is a significant scatter in the converged objective function values. We can therefore not be certain that global minima have been identified.

Another interesting observation, which can be made from Fig. 4, is the lack of correlation between the objective function value for the initial guess and for the final parameter values. Firstly, this indicates that it is not necessarily best to choose the starting guesses with the lowest objective function value. A good spread of the initial guesses in the parameter space might be more important. Secondly, it underlines the importance of having multiple initial guesses to improve the probability of locating parameter values at the global optimum.

The graphs used for evaluation of the objective function are shown in Fig. 5 for some of the studied models. It is clear that the most basic model type, AF, is unable to predict the biaxial deformation accurately (see Fig. 5a–d). By increasing the scale factor for the torque (α_T) relative to scale factor for the axial displacement ($\alpha_{\Delta L}$) in the objective function, a better fit for the torque can be obtained. It is, however, not possible for the AF models to fit both the torque and axial displacement accurately at the same time. As previously noted, based on the histogram in Fig. 4, adding more back-stresses does not solve this problem. The use of the combination of Armstrong–Frederick and Burlet–Cailletaud saturation in the BC2 model, gives a much better prediction at the cost of one additional material parameter. This is clearly seen when

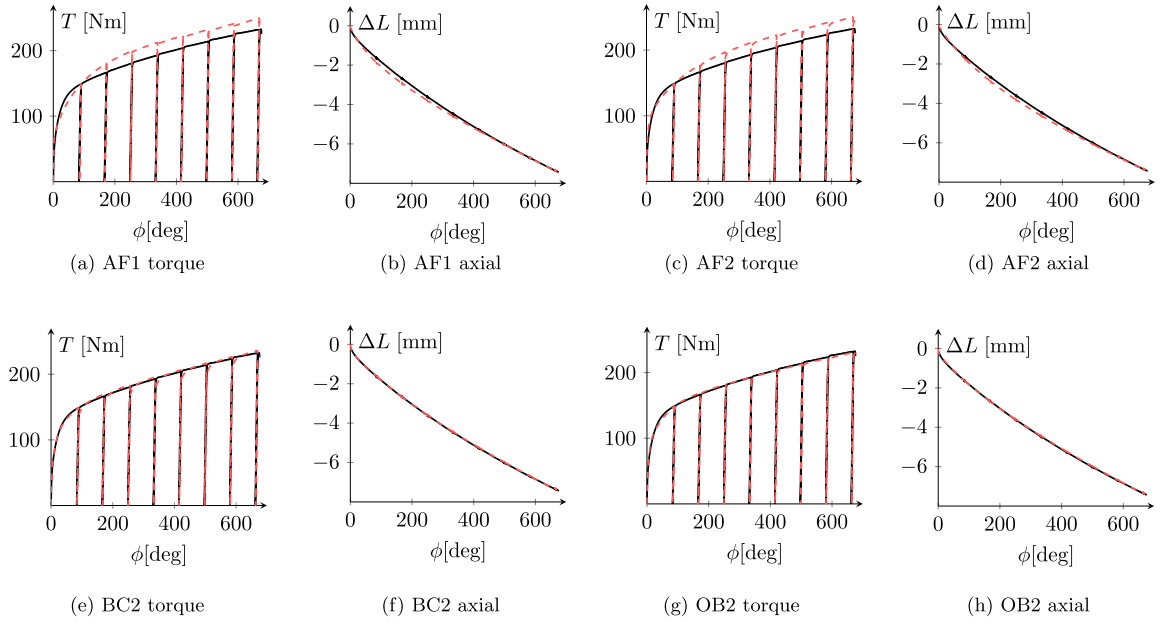

Fig. 5. Fitted material models for torque and axial displacement. Solid lines are values from experiment and dashed lines are simulated.

Table 4
Best optimization results for each model.

Model	E_{TOT}	Y_0	δ	H_{iso}	κ_∞	$H_{k,1}$	$Y_{k,1}$	$m_{k,1}$	$H_{k,2}$	$Y_{k,2}$	$m_{k,2}$
AF1	0.438	640	–	6270	0	1929	610	–	–	–	–
AF2	0.408	591	–	1037	1	1062	507	–	9878	177	–
BC1	0.162	483	0.329	219	157	5319	577	–	–	–	–
BC2	0.133	451	0.290	212	169	1450	293	–	10,148	322	–
OB1	0.184	529	0.599	85	508	2905	546	2.080	–	–	–
OB2	0.128	454	0.371	370	136	8921	302	2.580	1046	271	1.515
Unit	–	MPa	–	MPa	MPa	MPa	MPa	–	MPa	MPa	–

comparing the fits for the torque (e.g. compare Fig. 5c and e), as well when comparing the lowest objective function values in Table 4. The relative improvement by adding an additional back-stress in the BC model is larger than for the AF model. Furthermore, the Ohno–Wang model in combination with the Burlet–Cailletaud radial evanescence model with 2 back-stresses, OB2, also gives a very good agreement for both the torque and the axial displacement in Fig. 5g and h. Although the OB2 model obtains a slightly better fit of the data than the BC2 model, Table 4 shows that the BC1 model outperforms the OB1 model.

When using finite element simulations to fit the material parameters, the identifiability of the parameters can be an issue. Due to the complex loading paths (in contrast to uniaxial loading), it is rather certain that isotropic and kinematic hardening affect the results in different ways. Additionally, Fig. 7 shows that there is significant plasticity during the unloading, which further strengthens that the experiments can distinguish between isotropic and kinematic hardening.

5.2. Predictive abilities

From the fitted results, it is evident that the AF models are unable to predict the described biaxial loading. Hence, we choose to further investigate the ability of the BC2 and OB2 models to predict two additional loading cases, using the material parameters from Table 4. The loading case with the nominal axial load $\bar{P}_a = -600$ MPa, which is similar to the load case used for calibration, is evaluated first. The axial responses of the two models shown in Fig. 6b are almost identical, and predict the experimental data well. Furthermore, Fig. 6a shows that both models produce similar average torque levels during each cycle. After the elastic loading, the BC2 model seems to give a too high plastic modulus, which is compensated by an earlier yielding. The exponent m_i in the OB model allows for a response closer to the experimental (almost) bilinear behavior, i.e. a better prediction for the given loading is obtained. It should be noted that the material shows a weak rate dependence, and the careful observer may note a slight overshoot in the torque upon reloading stemming from this. The response for an experiment with a lower strain rate would likely match OB2 even better. Such an experiment has only been carried out for a nominal axial stress $\bar{P}_a = -500$ MPa, and only a qualitative evaluation is therefore possible for the other loading cases.

As $\bar{P}_a = -600$ MPa is quite similar to the nominal axial stress used for calibration, it is interesting to consider a completely different axial load. In Fig. 6c and d we therefore compare the model responses for the axial tensile load $\bar{P}_a = +250$ MPa. Both models predict the axial response reasonably well, but the BC2 model gives a slightly better fit. The torque response is generally over-predicted by the models. Towards the end of the second cycle the OB2 model exhibit some softening behavior, which is a combination of material softening and the reduced diameter due to the elongation. A much smaller torque reduction, 0.8 Nm, is observed in the experiment data before the specimen breaks. We can therefore conclude that the BC2 model performs slightly better for this load case. Although not shown here, similar conclusions can be

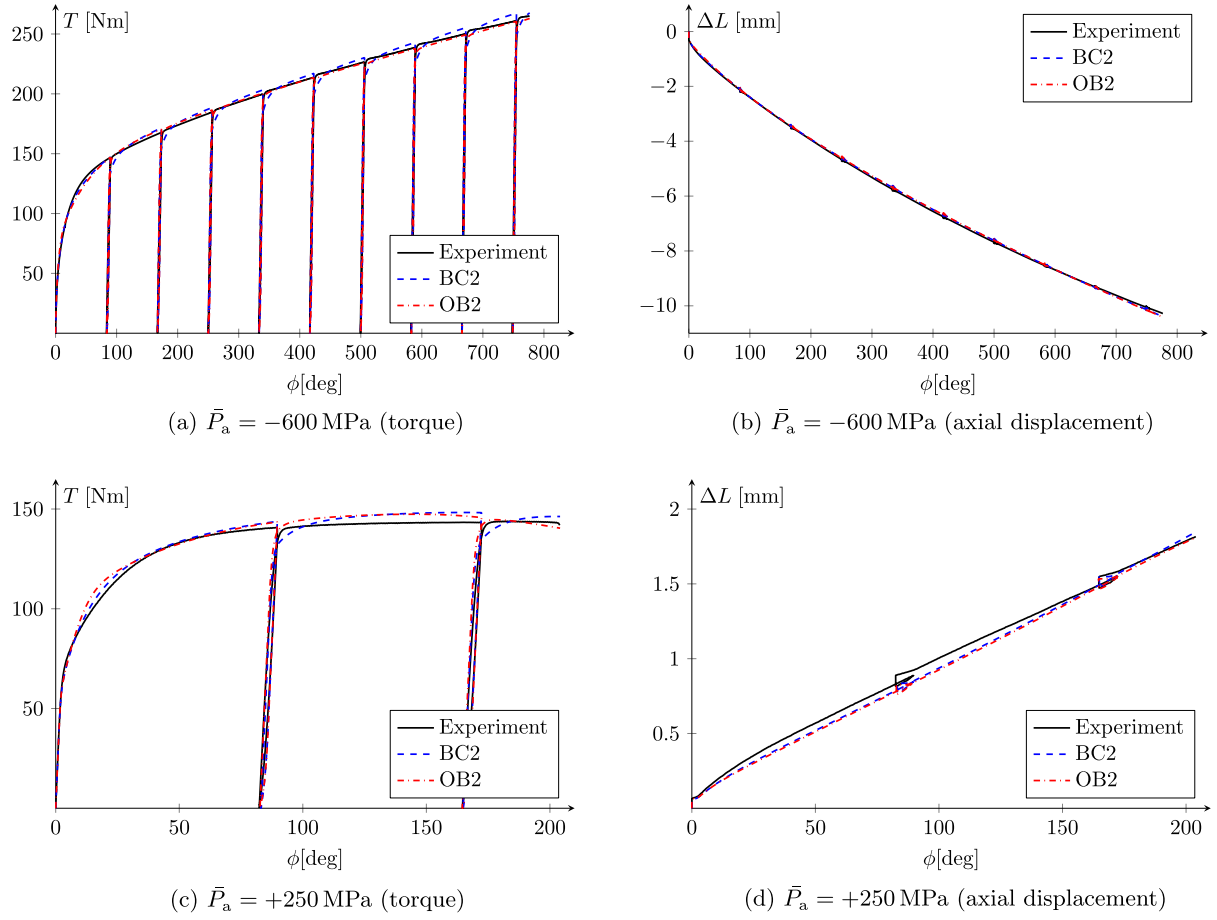

(a) $\bar{P}_a = -600$ MPa (torque) (b) $\bar{P}_a = -600$ MPa (axial displacement)

(c) $\bar{P}_a = +250$ MPa (torque) (d) $\bar{P}_a = +250$ MPa (axial displacement)

Fig. 6. Predictions for BC2 and OB2 models.

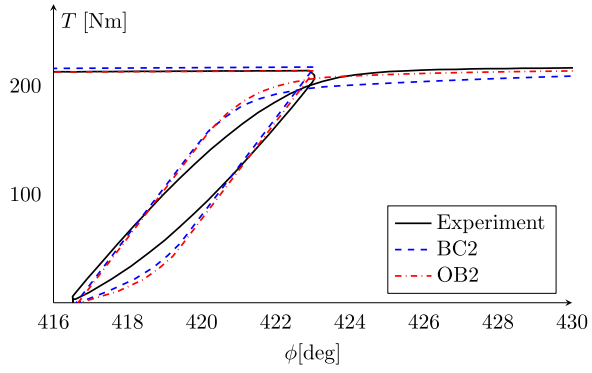

Fig. 7. Cyclic behavior at unloading/loading $\bar{P}_a = -600$ MPa.

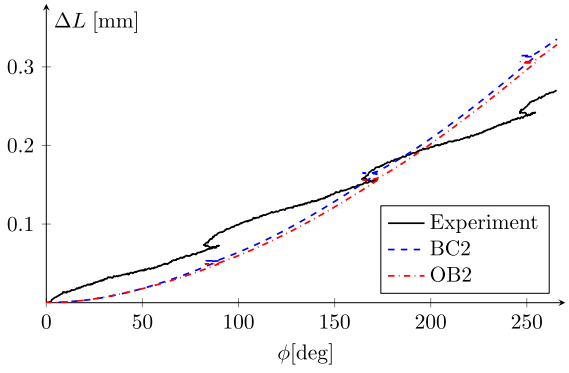

Fig. 8. Length changes for free end torsion ($\bar{P}_a = 0$ MPa).

drawn regarding the load case with an axial load $\bar{P}_a = -250$ MPa. Considering the minor differences between the results for the BC2 and OB2 models in Figs. 5 and 6, it cannot be concluded which model that is the better. The key finding is that both models, using two back-stresses, are able to both fit and predict the overall loads versus displacements in the considered experiments very well.

Fig. 7 shows that the models are not able to model the exact loop shape, but the locations of the endpoints are quite accurately predicted. The figure also clearly shows the Bauschinger effect, and this explains why the majority of the hardening is kinematic for the different models. This finding is supported by Johansson et al. (2006); Larijani et al. (2013), where the isotropic hardening was completely excluded due to its limited impact.

Regarding the free end torsion load case ($\bar{P}_a = 0$ MPa), none of the applied models are able to predict the axial response correctly, see Fig. 8. Due to the small length changes in free end torsion (known as the Swift effect: Swift, 1947), the relative uncertainty of the measured axial deformations is too large to make a conclusive comparison between the models. This is, however, an interesting load case for understanding the underlying mechanics, and the interested reader is referred to Wallin and Ristinmaa (2005). They extend the hyperelasto-plastic framework used in this paper, together with Armstrong–Frederick hardening, for modeling of the Swift effect.

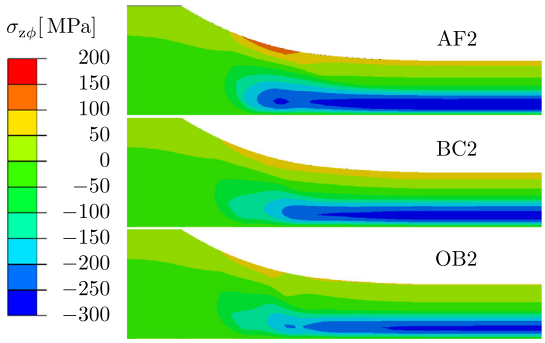

Fig. 9. Residual shear stress for calculating with a mesh size 0.3 mm and with material parameter values from Table 4, for the load case $\bar{P}_a = -500$ MPa. (For interpretation of the references to color in this figure legend, the reader is referred to the web version of this article.)

5.3. Influence of model choice on residual stresses

To further enhance the understanding of how the choice of model may affect the predicted mechanical response in the specimens, the residual stresses after the $\bar{P}_a = -500$ MPa load case are compared. The results for the AF2, BC2 and OB2 models are shown in Fig. 9, using the material parameters from Table 4. For these results we use a finer mesh, with one tenth of the element length used for the parameter identification in Section 5.1. This has a negligible effect on the torque and axial displacement curves (see Appendix B), but the stress field becomes better resolved. The AF2 model gives higher residual shear stresses, specifically close to the center of the specimen (blue) and at the surface in the radius transition (dark orange). Differences of similar magnitudes are observed for other stress measures. The BC2 model predicts higher stress than the OB2 model, even though their overall load versus displacement responses are similar. The choice of kinematic evolution laws has an influence on the residual stresses, and thereby influences the result of future evaluations of fatigue life.

6. Concluding remarks

Large shear strains in cylindrical test specimens have been achieved using an Axial-Torsion testing machine. The specimens were twisted more than 2 revolutions, while subjected to nominal axial compressive stress with magnitudes up to 600 MPa. The strain to failure is strongly increased with the amount of applied axial compressive stress, but this stress must be limited to avoid buckling of the specimens. During the twisting the specimen diameter increases and the length decreases significantly due to the large compressive loads.

The framework for hyperelasto-plasticity and kinematic hardening in Wallin et al. (2003) is used and extended to account for different kinematic evolution laws. Starting from several initial guesses, the Nelder–Mead Simplex optimization algorithm is used to fit the models to one experiment with a nominal axial compressive stress $\bar{P}_a = -500$ MPa. The models are finite element models of the specimens, which are differentiated by modifying the kinematic hardening in the material model. It is shown that the model with the standard Armstrong–Frederick type of dynamic recovery is unable to fit the biaxial material response accurately. The combination of either the Armstrong–Frederick or the Ohno–Wang kinematic hardening models with the Burlet–Cailletaud radial evanescence term, is shown to produce an excellent overall fit of the experimental data. Furthermore, these models are also able to very accurately predict the material responses for other load cases with different axial loads. The exception is the length change during free end torsion, i.e. the Swift effect, which is not predicted well by any of the considered models. Finally, investigating the predicted residual shear stresses revealed that the two latter models produce somewhat different residual stress states, even though their overall mechanical responses are similar.

A future step to improve the understanding of the material behavior during the large biaxial deformations, is to consider the local strain fields. This can be accomplished by using Digital Image Correlation (DIC) and thin-walled tubular specimens. Furthermore, such specimens will enable quantification of the previously discussed distortional hardening. Finally, predeformed hollow specimens can be used to investigate the low cycle fatigue behavior of the highly deformed material.

Acknowledgments

This work is part of the activities within the CHARMEC Centre of Excellence at Chalmers University of Technology. It is partly financed within the European Horizon 2020 Joint Technology Initiative Shift2Rail through contract no. 730841. The authors would like to thank voestalpine Schienen GmbH for supplying the specimen material and for fruitful discussions. Furthermore, the use of AceGen (Korelc, 2002) has been very effective in speeding up the implementation of material models. Finally, the material parameter optimization was performed on resources at Chalmers Centre for Computational Science and Engineering (C3SE) provided by the Swedish National Infrastructure for Computing (SNIC).

Appendix A. Machine calibration

In this appendix we briefly describe the methodology and results for the calibration of the biaxial test rig. Both the stiffness of the machine (axial and torsional) as well as the cross talk in the load sensing are analyzed. All test data presented and used previously in this paper have been compensated according to this methodology.

A1. Machine stiffness

The stiffness of the machine was measured using a 20 mm diameter bar manufactured from the same material and with the same grip distance of 75 mm as the specimen in Fig. 1. The deflections of the 75 mm portion of the bar were calculated and subtracted from the measured values, so that only the deflections of the machine were remaining.

A1.1. Axial stiffness

The deflections measured using the method described above for three different angular grip positions, are shown in Fig. 10. A linear regression gives an average stiffness of 200 kN/mm, which is lower than the 300 kN/mm axial stiffness of the specimen in Fig. 1. An accurate machine stiffness is therefore required to determine the specimen displacements. The linear regression model can capture the majority of the deflections, but there are some nonlinear hysteresis loops observed. The deviation from the calibrated stiffness is large for the first loading, and the subsequent ratcheting-like deflections are much smaller. It is therefore assumed that the majority of the nonlinear behavior is a function of the maximum applied load. The deviation of the deflection from the linear stiffness during the initial loading is therefore shown in Fig. 11.

From Fig. 11 it is clear that the inaccuracies increase substantially for loads above 40 kN, to more than 0.1 mm at 90 kN.

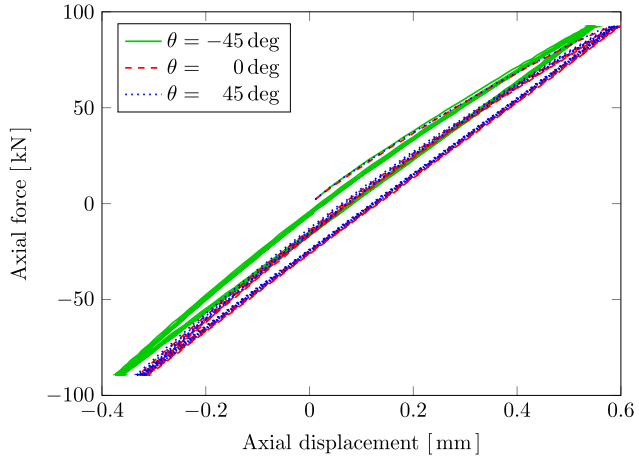

Fig. 10. Axial deflections.

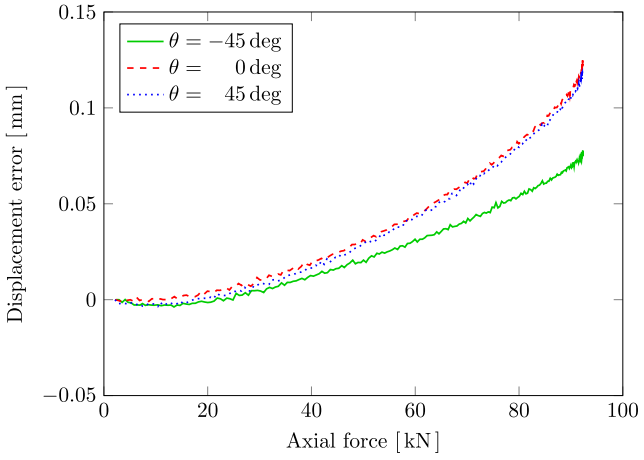

Fig. 11. Axial compensation error.

For loads below 40 kN the errors are in the order of 0.02 mm, which corresponds to the elastic deformation of the specimen at 6 kN. Although this force is quite high, during plastic deformation the specimen's secant stiffness is significantly reduced and hence the relative error decreases accordingly. We can therefore conclude that the accuracy of the axial position sensor is quite low for elastic loading, but rather good for plastic loading where displacements up to 10 mm occur.

A1.2. Torsional stiffness

Using the same method as for the axial displacements on the data depicted in Fig. 12, the obtained torsional stiffness is 466 Nm/deg. The torsional stiffness of the specimen in Fig. 1 is 29.2 Nm/deg, and hence the torsional deflections of the machine will be much smaller than the specimen deflections.

In the same fashion as for the axial response, the error of the compensated deflections are evaluated for different values of torque in Fig. 13. All curves are within ± 0.16 deg, which is approximately the elastic twist of the specimen at 5 Nm. From the same arguments as for the axial compensation error, the relative torque compensation error is reduced during plastic deformation. The torque in the experiments never exceeded 300 Nm, which gives a maximum compensation error of 0.11 deg, and hence the overall accuracy of the torsional rotation is quite good.

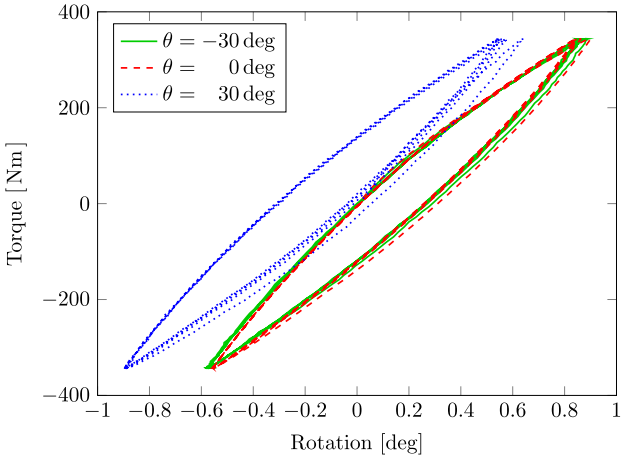

Fig. 12. Torsional deflections.

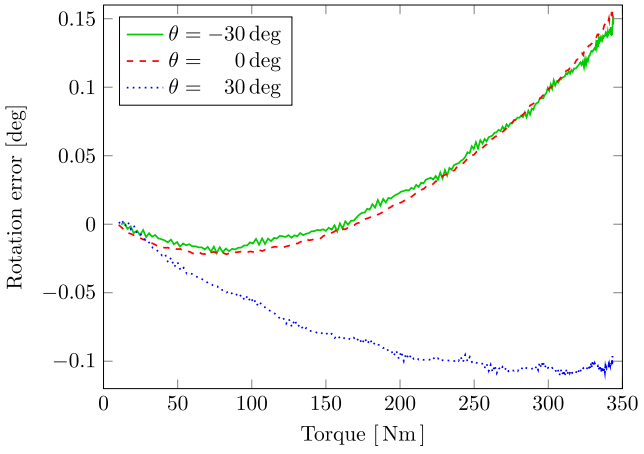

Fig. 13. Torsional compensation error.

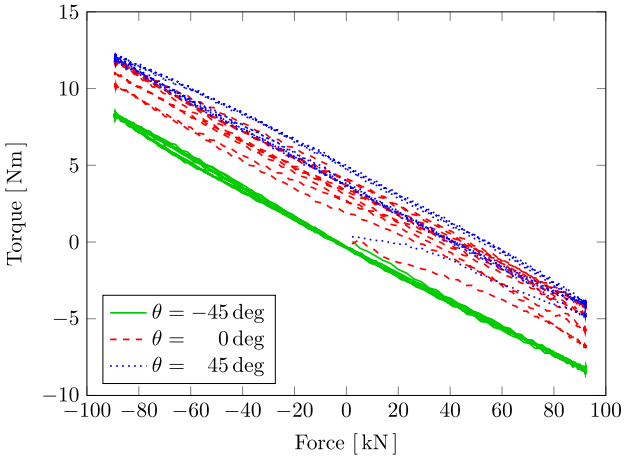

Fig. 14. Influence on torque measurements from axial load.

A2. Load sensor cross talk

Using the same measurements as above, considering how an axial load affects the measured torque during zero rotation, the response is shown in Fig. 14. Although the complete variation cannot be described using a linear regression model, the error can be significantly reduced by removing the fitted linear trend of -0.0904 Nm/kN.

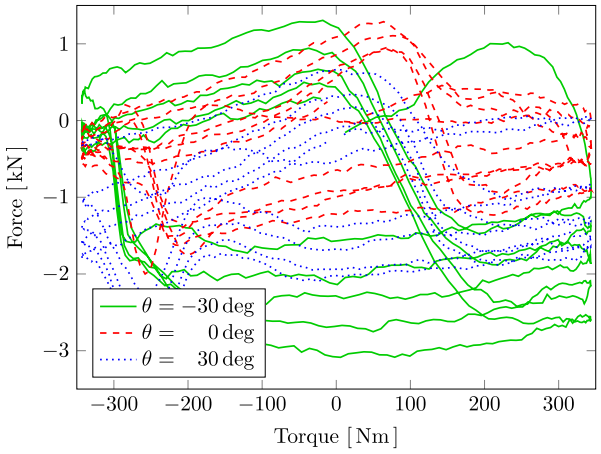

Fig. 15. Influence on force measurements from torsional load.

Considering the reverse effect, the influence of torque on the measured axial force, the results are shown in Fig. 15. No clear trends are present for this case, and no compensations are therefore made for the influence of torque on the measured axial force.

Appendix B. Mesh and time step sensitivity

The torque response for a simulation with the mesh size used in the present study (see Fig. 3) is compared with the response for a much finer mesh. A small part of the torque response is evaluated in Fig. 16a to highlight any differences. The differences in maximum torque and length change for the full simulation are 0.025% and 0.028% respectively. We therefore conclude that the 3.0 mm mesh provides sufficient accuracy for the present study.

When the backward Euler integration scheme is used for the finite strain frameworks, Vladimirov et al. (2008) found that the solution can be quite dependent on the time step size. We therefore compare the simulated mechanical response for a simulation with ten times the number of time steps that was chosen in the present paper. At the zoom level in Fig. 16b the graphs almost coincide, but the differences are larger than for the mesh comparison in Fig. 16b. This becomes apparent when comparing the maximum torque and length change, giving differences of 0.038% and 0.11% respectively. The length change is affected more by the larger time step than by a larger mesh. However, comparing to the uncertainty of the experimental measurements (see Appendix A), the modeling errors are acceptable.

References

Abdel-Karim, M., 2009. Modified kinematic hardening rules for simulations of ratchetting. Int. J. Plast. 25 (8), 1560–1587. doi:10.1016/j.ijplas.2008.10.004.

Abdel-Karim, M., Ohno, N., 2000. Kinematic hardening model suitable for ratchetting with steady-state. Int. J. Plast. 16 (3), 225–240. doi:10.1016/S0749-6419(99)00052-2.

Alwahdi, F.A.M., Kapoor, A., Franklin, F.J., 2013. Subsurface microstructural analysis and mechanical properties of pearlitic rail steels in service. Wear 302 (1–2), 1453–1460. doi:10.1016/j.wear.2012.12.058.

Bari, S., Hassan, T., 2002. An advancement in cyclic plasticity modeling for multiaxial ratcheting simulation. Int. J. Plast. 18 (7), 873–894. doi:10.1016/S0749-6419(01)00012-2.

Barthel, C., Levkovitch, V., Svendsen, B., 2008. Modeling of sheet metal forming processes taking into account distortional hardening. Int. J. Mater. Form. 1 (SUPPL. 1), 105–108. doi:10.1007/s12289-008-0035-y.

Brommesson, R., Ekh, M., Hörnqvist, M., 2015. Correlation between crack length and load drop for low-cycle fatigue crack growth in Ti-6242. Int. J. Fatigue 81, 1–9. doi:10.1016/j.ijfatigue.2015.07.006.

Burlet, H., Cailletaud, G., 1986. Numerical techniques for cyclic plasticity at variable temperature. Eng. Comput. 3 (2), 143–153. doi:10.1108/eb023652.

Chaboche, J., 1986. Time-independent constitutive theories for cyclic plasticity. Int. J. Plast. 2 (2), 149–188. doi:10.1016/0749-6419(86)90010-0.

Chen, X., Jiao, R., Kim, K., 2003. Simulation of ratcheting strain to a high number of cycles under biaxial loading. Int. J. Solids Struct. 40 (26), 7449–7461. doi:10.1016/j.ijsolstr.2003.08.009.

Chen, X., Jiao, R., Kim, K.S., 2005. On the Ohno–Wang kinematic hardening rules for multiaxial ratcheting modeling of medium carbon steel. Int. J. Plast. 21 (1), 161–184. doi:10.1016/j.ijplas.2004.05.005.

Cvetkovski, K., Ahlström, J., 2013. Characterisation of plastic deformation and thermal softening of the surface layer of railway passenger wheel treads. Wear 300 (1–2), 200–204. doi:10.1016/j.wear.2013.01.094.

Delobelle, P., Robinet, P., Bocher, L., 1995. Experimental study and phenomenological modelization of ratchet under uniaxial and biaxial loading on an austenitic stainless steel. Int. J. Plast. 11 (4), 295–330. doi:10.1016/S0749-6419(95)00001-1.

Dettmer, W., Reese, S., 2004. On the theoretical and numerical modelling of Armstrong–Frederick kinematic hardening in the finite strain regime. Comput. Methods Appl. Mech. Eng. 193 (1), 87–116. doi:10.1016/j.cma.2003.09.005.

Draï, A., Aour, B., 2013. Analysis of plastic deformation behavior of HDPE during high pressure torsion process. Eng. Struct. 46, 87–93. doi:10.1016/j.engstruct.2012.06.033.

Ekh, M., 2001. Thermo-Elastic-Viscoplastic modeling of IN792. J. Mech. Behav. Mater. 12 (6), 359–388. doi:10.1515/JMBM.2001.12.6.359.

Estrin, Y., Molotnikov, a., Davies, C.H.J., Lapovok, R., 2008. Strain gradient plasticity modelling of high-pressure torsion. J. Mech. Phys. Solids 56 (4), 1186–1202. doi:10.1016/j.jmps.2007.10.004.

Feigenbaum, H.P., Dafalias, Y.F., 2007. Directional distortional hardening in metal plasticity within thermodynamics. Int. J. Solids Struct. 44 (22–23), 7526–7542. doi:10.1016/j.ijsolstr.2007.04.025.

Frederick, C.O., Armstrong, P.J., 2007. A mathematical representation of the multiaxial Bauschinger effect. Mater. High Temp. 24 (1), 1–26. doi:10.1179/096034007X207589.

Harrysson, M., Harrysson, A., Ristinmaa, M., 2007. Spatial representation of evolving anisotropy at large strains. Int. J. Solids Struct. 44 (10), 3514–3532. doi:10.1016/j.ijsolstr.2006.10.002.

Hassan, T., Corona, E., Kyriakides, S., 1992. Ratcheting in cyclic plasticity, part II: Multiaxial behavior. Int. J. Plast. 8 (2), 117–146. doi:10.1016/0749-6419(92)90010-A.

Hohenwarter, a., Taylor, a., Stock, R., Pippan, R., 2011. Effect of large shear deformations on the fracture behavior of a fully pearlitic steel. Metall. Mater. Trans. A 42 (6), 1609–1618. doi:10.1007/s11661-010-0541-7.

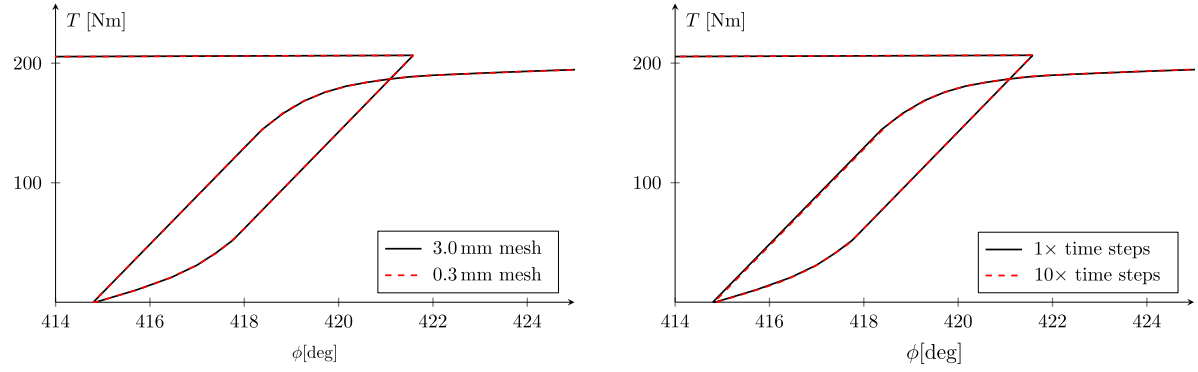

(a) Effect of different mesh sizes

(b) Effect of different number of time steps

Fig. 16. Investigation of simulation parameters.

Ivanisenko, Y.V., Valiev, R., Lojkowski, W., Grob, A., Fecht, H.-J., 2002. Nanostructure Formation and Carbides Dissolution in Rail Steel Deformed by High Pressure Torsion. In: Zhu, Y., Langdon, T., Mishra, R., Setniatin, S., Saran, M., Lowe, T. (Eds.), Ultrafine Grained Materials II. John Wiley & Sons, Inc, Hoboken, NJ, USA., pp. 47–54. chapter 6. doi:10.1002/9781118804537.ch6.

Johansson, G., Ahlström, J., Ekh, M., 2006. Parameter identification and modeling of large ratcheting strains in carbon steel. Comput. Struct. 84 (15–16), 1002–1011. doi:10.1016/j.compstruc.2006.02.016.

Johansson, G., Ekh, M., Runesson, K., 2005. Computational modeling of inelastic large ratcheting strains. Int. J. Plast. 21 (5), 955–980. doi:10.1016/j.ijplas.2004.05.013.

Johansson, G., Menzel, A., Runesson, K., 2005. Modeling of anisotropic inelasticity in pearlitic steel at large strains due to deformation induced substructure evolution. Eur. J. Mech. A. Solids 24 (6), 899–918. doi:10.1016/j.euromechsol.2005.06.006.

Johnson, K., 1989. The strength of surfaces in rolling contact. J. Mech. Eng. Sci. 203 (December 1988), 151–163.

Khoddam, S., Shamdani, A.H., Mutton, P., Ravitharan, R., Beynon, J.H., Kapoor, A., 2014. A new test to study the cyclic hardening behaviour of a range of high strength rail materials. Wear 313 (1–2), 43–52. doi:10.1016/j.wear.2014.02.012.

Kim, H.S., 2001. Finite element analysis of high pressure torsion processing. J. Mater. Process. Technol. 113 (1–3), 617–621. doi:10.1016/S0924-0136(01)00709-9.

Korelc, J., 2002. Multi-language and multi-environment generation of nonlinear finite element codes. Eng. Comput. 18 (4), 312–327. doi:10.1007/s003660200028.

Lagarias, J.C., Reeds, J.A., Wright, M.H., Wright, P.E., 1998. Convergence Properties of the Nelder–Mead Simplex Method in Low Dimensions. SIAM J. Optim. 9 (1), 112–147. doi:10.1137/S1052623496303470.

Larijani, N., Johansson, G., Ekh, M., 2013. Hybrid micro-macromechanical modeling of anisotropy evolution in pearlitic steel. Eur. J. Mech. A. Solids 38, 38–47. doi:10.1016/j.euromechsol.2012.09.011.

Larijani, N., Kammerhofer, C., Ekh, M., 2015. Simulation of high pressure torsion tests of pearlitic steel. J. Mater. Process. Technol. 223, 337–343. doi:10.1016/j.jmatprotec.2015.04.018.

Lion, A., 2000. Constitutive modelling in finite thermoviscoplasticity: a physical approach based on nonlinear rheological models. Int. J. Plast. 16 (5), 469–494. doi:10.1016/S0749-6419(99)00038-8.

Menzel, A., Steinmann, P., 2003. On the spatial formulation of anisotropic multiplicative elasto-plasticity. Comput. Methods Appl. Mech. Eng. 192 (31–32), 3431–3470. doi:10.1016/S0045-7825(03)00353-0.

Meyer, K.A., Ekh, M., 2017. A comparison of two frameworks for kinematic hardening in hyperelasto-plasticity. In: Computational Plasticity XIV: Fundamentals and Applications - Proceedings of the 14th International Conference on Computational Plasticity - Fundamentals and Applications, COMPLAS 2017.

Ohno, N., Wang, J.-D., 1993. Kinematic hardening rules with critical state of dynamic recovery, part I: formulation and basic features for ratchetting behavior. Int. J. Plast. 9 (3), 375–390. doi:10.1016/0749-6419(93)90042-O.

Ohno, N., Wang, J.-D., 1993. Kinematic hardening rules with critical state of dynamic recovery, part II: application to experiments of ratchetting behavior. Int. J. Plast. 9 (3), 391–403. doi:10.1016/0749-6419(93)90043-P.

Pietryga, M.P., Vladimirov, I.N., Reese, S., 2012. A finite deformation model for evolving flow anisotropy with distortional hardening including experimental validation. Mech. Mater. 44, 163–173. doi:10.1016/j.mechmat.2011.07.014.

Plesek, J., Feigenbaum, H.P., Dafalias, Y.F., 2010. Convexity of yield surface with directional distortional hardening rules. J. Eng. Mech. 136 (4), 477–484. doi:10.1061/(ASCE)EM.1943-7889.0000077.

Portier, L., Calloch, S., Marquis, D., Geyer, P., 2000. Ratchetting under tension-torsion loadings: experiments and modelling. Int. J. Plast. 16 (3), 303–335. doi:10.1016/S0749-6419(99)00056-X.

Shi, B., Bartels, A., Mosler, J., 2014. On the thermodynamically consistent modeling of distortional hardening: a novel generalized framework. Int. J. Plast. 63, 170–182. doi:10.1016/j.ijplas.2014.05.008.

Sung, S.-J., Liu, L.-W., Hong, H.-K., Wu, H.-C., 2011. Evolution of yield surface in the 2D and 3D stress spaces. Int. J. Solids Struct. 48 (6), 1054–1069. doi:10.1016/j.ijsolstr.2010.12.011.

Swift, H.W., 1947. Length changes in metals under torsional overstrain. Engineering 163, 253–257.

Vladimirov, I.N., Pietryga, M.P., Reese, S., 2008. On the modelling of non-linear kinematic hardening at finite strains with application to springback - Comparison of time integration algorithms. Int. J. Numer. Methods Eng. 75 (1), 1–28. doi:10.1002/nme.2234.

Wallin, M., Ristinmaa, M., 2005. Deformation gradient based kinematic hardening model. Int. J. Plast. 21 (10), 2025–2050. doi:10.1016/j.ijplas.2005.01.007.

Wallin, M., Ristinmaa, M., Ottosen, N.S., 2003. Kinematic hardening in large strain plasticity. Eur. J. Mech. A. Solids 22 (3), 341–356. doi:10.1016/S0997-7538(03)00026-3.

Wei, P.T., Lu, C., Tieu, K., Deng, G.Y., 2014. A study of plastic deformation behavior during high pressure torsion process by crystal plasticity finite element simulation. IOP Conf. Ser.: Mater. Sci. Eng. 63, 012045. doi:10.1088/1757-899X/63/1/012045.

Wetscher, F., Stock, R., Pippan, R., 2007. Changes in the mechanical properties of a pearlitic steel due to large shear deformation. Mater. Sci. Eng. A 445–446, 237–243. doi:10.1016/j.msea.2006.09.026.

Yoon, S.C., Horita, Z., Kim, H.S., 2008. Finite element analysis of plastic deformation behavior during high pressure torsion processing. J. Mater. Process. Technol. 201 (1–3), 32–36. doi:10.1016/j.jmatprotec.2007.11.204.

Zhu, Y., Kang, G., Kan, Q., Yu, C., Ding, J., 2013. An extended cyclic plasticity model at finite deformations describing the Bauschinger effect and ratchetting behavior. In: 13th International Conference on Fracture 2013, ICF 2013, 5, pp. 1–11.